

See discussions, stats, and author profiles for this publication at: <https://www.researchgate.net/publication/44574248>

# Photoelectrochemical Water Splitting with Mesoporous Hematite Prepared by a Solution-Based Colloidal Approach

ARTICLE in JOURNAL OF THE AMERICAN CHEMICAL SOCIETY · JUNE 2010

Impact Factor: 12.11 · DOI: 10.1021/ja101564f · Source: PubMed

CITATIONS

356

READS

44

8 AUTHORS, INCLUDING:



**Radek Zboril**

Palacký University of Olomouc

285 PUBLICATIONS 6,558 CITATIONS

SEE PROFILE



**Florian Le Formal**

École Polytechnique Fédérale de Lausanne

29 PUBLICATIONS 2,175 CITATIONS

SEE PROFILE



**Rosa Robert**

Paul Scherrer Institut

46 PUBLICATIONS 1,067 CITATIONS

SEE PROFILE



**Anke Weidenkaff**

Universität Stuttgart

295 PUBLICATIONS 3,510 CITATIONS

SEE PROFILE

### Photoelectrochemical Water Splitting with Mesoporous Hematite Prepared by a Solution-Based Colloidal Approach

Kevin Sivula,<sup>\*,†</sup> Radek Zboril,<sup>‡</sup> Florian Le Formal,<sup>†</sup> Rosa Robert,<sup>§</sup> Anke Weidenkaff,<sup>§</sup> Jiri Tucek,<sup>‡</sup> Jiri Frydrych,<sup>‡</sup> and Michael Grätzel<sup>†</sup>

*Institut des Sciences et Ingénierie Chimiques, Ecole Polytechnique Fédérale de Lausanne, Laboratory of Photonics and Interfaces, Station 6, CH-1015 Lausanne, Switzerland, Department of Physical Chemistry & Nanomaterials Research Centre, Palacky University, Svobody 26, 77146 Olomouc, Czech Republic, and Solid State Chemistry and Analyses Laboratory EMPA, the Swiss Federal Laboratories for Materials Testing and Research EMPA, CH-8600 Duebendorf, Switzerland*

Received February 23, 2010; E-mail: kevin.sivula@epfl.ch

**Abstract:** Sustainable hydrogen production through photoelectrochemical water splitting using hematite ( $\alpha\text{-Fe}_2\text{O}_3$ ) is a promising approach for the chemical storage of solar energy, but is complicated by the material's nonoptimal optoelectronic properties. Nanostructuring approaches have been shown to increase the performance of hematite, but the ideal nanostructure giving high efficiencies for all absorbed light wavelengths remains elusive. Here, we report for the first time mesoporous hematite photoelectrodes prepared by a solution-based colloidal method which yield water-splitting photocurrents of  $0.56\text{ mA cm}^{-2}$  under standard conditions (AM 1.5G  $100\text{ mW cm}^{-2}$ ,  $1.23\text{ V}$  vs reversible hydrogen electrode, RHE) and over  $1.0\text{ mA cm}^{-2}$  before the dark current onset ( $1.55\text{ V}$  vs RHE). The sintering temperature is found to increase the average particle size, and have a drastic effect on the photoactivity. X-ray photoelectron spectroscopy and magnetic measurements using a SQUID magnetometer link this effect to the diffusion and incorporation of dopant atoms from the transparent conducting substrate. In addition, examining the optical properties of the films reveals a considerable change in the absorption coefficient and onset properties, critical aspects for hematite as a solar energy converter, as a function of the sintering temperature. A detailed investigation into hematite's crystal structure using powder X-ray diffraction with Rietveld refinement to account for these effects correlates an increase in a  $C_{3v}$ -type crystal lattice distortion to the improved optical properties.

#### Introduction

Because of its chemical stability, widespread availability, and capability to absorb photons in the visible spectral range (band gap,  $E_g = 2.0\text{ eV}$ ), hematite ( $\alpha\text{-Fe}_2\text{O}_3$ ) is a promising material for the sustainable and carbon neutral storage of solar energy by the photoelectrochemical (PEC) splitting of water into hydrogen and oxygen.<sup>1</sup> The unassisted solar production of hydrogen can be accomplished using only water and sunlight as inputs with hematite as a photoanode in a tandem cell configuration.<sup>2</sup> However, since the photon penetration depth at visible wavelengths in hematite ( $\alpha^{-1} = 118\text{ nm}$  at  $\lambda = 550\text{ nm}$ ) causes the majority of photogenerated carriers to be produced at a distance on the order of  $100\text{ nm}$  from the semiconductor liquid junction (SCLJ),<sup>3</sup> and the ultrafast recombination of the photogenerated carriers (time constants on

the order of  $10\text{ ps}$ )<sup>4</sup> along with the poor minority charge carrier mobility ( $0.2\text{ cm}^2\text{ V}^{-1}\text{ s}^{-1}$ )<sup>5</sup> leads to a hole diffusion length,  $L_D$ , of only  $2\text{--}4\text{ nm}$ , the overall photocurrents produced by solar light have been severely limited.<sup>6</sup> In spite of this, recent efforts by many groups to nanostructure  $\text{Fe}_2\text{O}_3$  have resulted in significant advances in the visible light response by increasing the surface area of the hematite exposed to the aqueous electrolyte.<sup>7–9</sup> For example, a very successful system is the silicon doped cauliflower-type  $\text{Fe}_2\text{O}_3$  prepared by atmospheric pressure chemical vapor deposition (APCVD) in our laboratories.<sup>10</sup> These photoanodes supply a state-of-the-art  $2.2\text{ mA cm}^{-2}$  photocurrent at  $1.23\text{ V}$  versus the reversible hydrogen electrode (RHE) in  $1\text{ M NaOH}$  at standard solar conditions (AM 1.5 G

<sup>†</sup> Laboratory of Photonics and Interfaces.

<sup>‡</sup> Palacky University.

<sup>§</sup> Solid State Chemistry and Analyses Laboratory EMPA.

(1) Lindgren, T.; Vayssieres, L.; Wang, H.; Lindquist, S. E. *Chem. Phys. Nanostruct. Semicond.* **2003**, *83*.

(2) Brillet, J.; Cornuz, M.; Le Formal, F.; Yum, J. H.; Grätzel, M.; Sivula, K. *J. Mater. Res.* **2010**, *25*, 17.

(3) Itoh, K.; Bockris, J. O. J. *Electrochem. Soc.* **1984**, *131*, 1266.

(4) Cherepy, N. J.; Liston, D. B.; Lovejoy, J. A.; Deng, H. M.; Zhang, J. Z. *J. Phys. Chem. B* **1998**, *102*, 770.

(5) Bosman, A. J.; Vandaal, H. J. *Adv. Phys.* **1970**, *19*, 1.

(6) Kennedy, J. H.; Frese, K. W. *J. Electrochem. Soc.* **1978**, *125*, 709.

(7) Alexander, B. D.; Kulesza, P. J.; Rutkowska, L.; Solarska, R.; Augustynski, J. *J. Mater. Chem.* **2008**, *18*, 2298.

(8) van de Krol, R.; Liang, Y. Q.; Schoonman, J. J. *J. Mater. Chem.* **2008**, *18*, 2311.

(9) Sartoretti, C. J.; Ulmann, M.; Alexander, B. D.; Augustynski, J.; Weidenkaff, A. *Chem. Phys. Lett.* **2003**, *376*, 194.

(10) Cesar, L.; Kay, A.; Martinez, J. A. G.; Grätzel, M. *J. Am. Chem. Soc.* **2006**, *128*, 4582.

100 mW cm<sup>-2</sup>).<sup>11</sup> This performance corresponds to a 3.3% solar-to-hydrogen efficiency in a tandem cell configuration,<sup>12</sup> and while promising, this value lies considerably below the ca. 16% efficiency predicted with a material of band gap of 2.0 eV.<sup>13</sup> We have since shown that, despite the improvement offered by the cauliflower-type structure, a main limitation of these photoanodes remains the morphology; the relatively thick core of the cauliflower-type structure leaves a substantial amount of the material at a distance many times  $L_D$  from the SCLJ. This causes absorbed photons with wavelengths near the band edge (450 nm <  $\lambda$  < 600 nm) to exhibit absorbed-photon-to-current efficiencies (APCEs) below 20%.<sup>14</sup> While this limitation can be conceptually improved by coating an extremely thin film of hematite on a rough, nanostructured support in a host-scaffold/guest absorber approach,<sup>15</sup> ultrathin films of hematite (<20 nm) suffer from limited performance due to increased recombination of carriers at the interface.<sup>16,17</sup> A better morphology for hematite would be one with a sufficient thickness to absorb all possible solar irradiation and that intentionally positions all of the Fe<sub>2</sub>O<sub>3</sub> within one or two  $L_D$  (<10 nm) from the SCLJ. In addition, for the tandem cell device geometry, hematite should be deposited on an optically transparent substrate to allow photons with energy less than the band gap to be transmitted to another light absorber, and in order to be technologically suitable, any preparation method for this material must be as economical as possible.

Solution-based colloidal methods for preparing oxide semiconductor electrodes allow the use of inexpensive processing techniques like spin-coating or doctor-blading and can give mesoporous thin films with a morphology placing all of the material within high proximity to the SCLJ. The prototypical example of this approach is the mesoporous TiO<sub>2</sub> used in the champion dye-sensitized solar cells.<sup>18</sup> Indeed, this method was first reported for hematite by Bjorksten et al. in 1994.<sup>19</sup> Here, micrometer-thick porous thin films of necked hematite were observed to have good adhesion to the substrate and a primary particle size in the 25–75 nm range. However the APCE of these photoanodes for water splitting was quite low, less than 1% at 1.4 V versus RHE in 0.1 M NaOH with 400 nm incident irradiation. Charge carrier recombination was found to be the controlling factor for the photocurrent. The higher quantum efficiency of similarly prepared particles independent from a mesoporous thin film geometry (simply dispersed in electrolyte) suggested the grain boundaries between the particles were the cause of the recombination and poor performance.<sup>20</sup> This limitation was addressed by Qian et al. through altering the film thickness to optimize the light absorption/carrier transport issue.<sup>21</sup> However, no significant improvement was obtained.

Despite the poor performance of hematite photoanodes prepared by colloidal methods, their potential to allow the easily scalable and inexpensive preparation of hematite with the ideal nanostructured morphology motivated our continued efforts. Here, we report for the first time mesoporous hematite films prepared by doctor blading colloidal solutions including a porogen that can achieve water splitting photocurrents up to 1 mA cm<sup>-2</sup> under standard testing conditions. This drastic improvement has been enabled by optimizing the sintering temperature, which is found to facilitate the incorporation of dopant atoms. Investigations into the change of optical properties induced by the temperature treatment further suggest a structural relaxation of the crystal lattice may play an important role with photoactivity in hematite.

## Experimental Methods

**Preparation of Mesoporous Thin Films.** About 400 mg of dry Fe<sub>2</sub>O<sub>3</sub> nanopowder prepared by the thermal decomposition of Fe(CO)<sub>5</sub> (ca. 10 nm d., provided generously by BASF) was combined using a mortar and pestle with 40  $\mu$ L of a 10% solution of acetylacetone (Acac) in 1-hexanol until all of the powder was incorporated into a paste. Here, the hexanol was used to slow solvent evaporation and the Acac was used as a nanoparticle capping surfactant. The nanoparticle paste was then diluted with 1% Acac in 2-propanol by adding 100  $\mu$ L fractions until 5 mL. This dispersion was sonicated by an ultrasonic tip sonicator (Branson Sonifier 250) in a temperature controlled water-bath (10 °C) at a 20% duty cycle for 5 min. This solution was concentrated by evaporation to 22 mg/mL measured by evaporating a known volume of solution and weighing the solids. The nanoparticle solution was combined with a 4 wt % solution of hydroxypropyl cellulose (HPC) in 2-propanol in order to have a 30 wt % HPC based on solid content and further diluted with 2-propanol (to a final concentration of 9.4 mg/mL based on total solids) to prevent the gelling of the colloid. Substrates were prepared with fused quartz microscope slides (Ted Pella) and coated with F:SnO<sub>2</sub> by the flash CVD of SnCl<sub>4</sub> and NH<sub>4</sub>F or the sputtering of 20 nm Ti followed by 200 nm Pt. The final colloid solution containing the porogen was then coated onto the substrate via doctor-blading with a 40  $\mu$ m invisible tape (3M) as a spacer. These films were air-dried for 30 min before the initial heating to remove the organics (1.5 °C min<sup>-1</sup> to 400 °C, 10 h) and the samples were cooled before the second heat treatment in a tube furnace (2 in d.) at a set point of 700 or 800 °C. A thermocouple placed in the tube at the same position of the samples verified the set point temperature within 5 °C.

**Photoelectrochemical Characterization.** Photocurrent measurements were performed to estimate the solar photocurrent of the photoanodes in a three-electrode configuration with 1 M NaOH (pH 13.6) as electrolyte using Ag/AgCl in saturated KCl as a reference electrode. The hematite electrode was scanned at 50 mV s<sup>-1</sup> between -300 and 800 mV versus Ag/AgCl. The potential is reported relative to the reversible hydrogen electrode potential (RHE). The samples were illuminated (area = 0.5 cm<sup>2</sup>) with simulated sunlight from a 450 W xenon lamp (Osram, ozone free) using a KG3 filter (3 mm, Schott) with a measured intensity of 1 sun (100 mW cm<sup>-2</sup>, spectrally corrected) at the sample face.

**Scanning Electron Microscopy (SEM).** The morphology of the mesoporous hematite thin films were characterized using a high-resolution scanning electron microscope (FEI XL30 SFEG). The acceleration voltage was 5 keV, while an in-lens detector was employed with a working distance of 5 mm. The samples were investigated after the photoelectrochemical measurements and sample positions coincided with the illuminated area.

**UV–Vis Absorbance.** The absorbance spectra were taken with a Varian Cary 5 spectrophotometer fitted with an 11 cm diameter integrating sphere coated with polytetrafluoroethylene (PTFE). This setup allowed measuring the total transmittance and the total reflectance of samples of interest. The absorption was calculated

- (11) Kay, A.; Cesar, I.; Gratzel, M. *J. Am. Chem. Soc.* **2006**, *128*, 15714.
- (12) Duret, A.; Gratzel, M. *J. Phys. Chem. B* **2005**, *109*, 17184.
- (13) Murphy, A. B.; Barnes, P. R. F.; Randeniya, L. K.; Plumb, I. C.; Grey, I. E.; Horne, M. D.; Glasscock, J. A. *Int. J. Hydrogen Energy* **2006**, *31*, 1999.
- (14) Cesar, I.; Sivula, K.; Kay, A.; Zboril, R.; Gratzel, M. *J. Phys. Chem. C* **2009**, *113*, 772.
- (15) Sivula, K.; Le Formal, F.; Gratzel, M. *Chem. Mater.* **2009**, *21*, 2862.
- (16) Itoh, K.; Bockris, J. O. J. *Appl. Phys.* **1984**, *56*, 874.
- (17) Liang, Y. Q.; Enache, C. S.; van de Krol, R. *Int. J. Photoenergy* **2008**, 739864.
- (18) Nazeeruddin, M. K.; De Angelis, F.; Fantacci, S.; Selloni, A.; Viscardi, G.; Liska, P.; Ito, S.; Takeru, B.; Gratzel, M. *J. Am. Chem. Soc.* **2005**, *127*, 16835.
- (19) Bjorksten, U.; Moser, J.; Gratzel, M. *Chem. Mater.* **1994**, *6*, 858.
- (20) Moser, J.; Gratzel, M. *Helv. Chim. Acta* **1982**, *65*, 1436.
- (21) Qian, X.; Zhang, X.; Bai, Y.; Li, T.; Tang, X.; Wang, E.; Dong, S. *J. Nanopart. Res.* **2000**, *2*, 191.

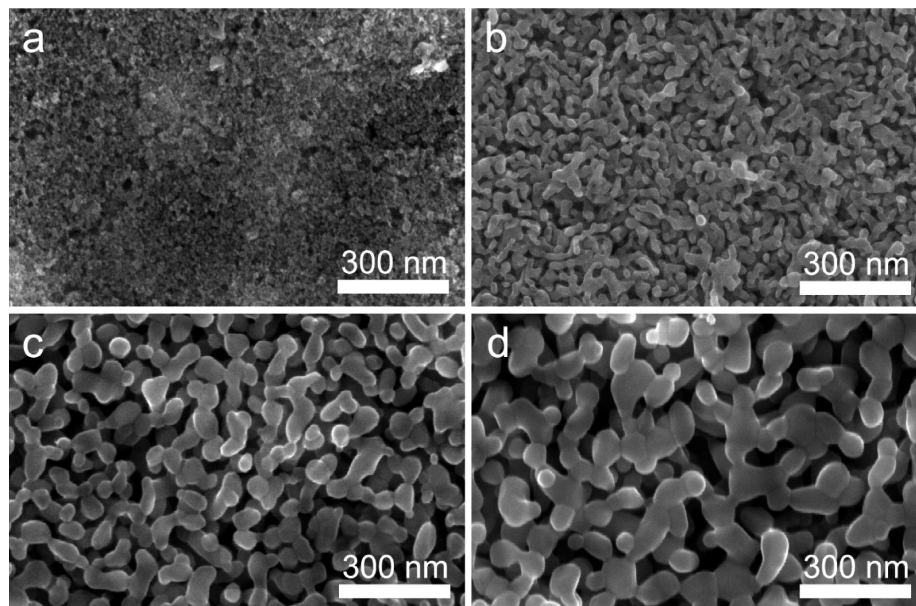


**Figure 1.** Scanning electron micrographs of mesoporous hematite films prepared on  $\text{SiO}_2/\text{F}:\text{SnO}_2$  substrates after different heat treatments: (a) as deposited with porogen, (b) after 10 h at 400 °C, and after 20 min at 700 °C (c) and 800 °C (d).

from these measurements with the formula  $A = -\log(T + R)$ , where  $A$  is the absorbance,  $T$  is the total transmittance, and  $R$  is the total reflectance. The thickness of the hematite film as determined by AFM (and corrected for porosity) was used to calculate the absorption coefficient using  $A = \alpha' t$ , where  $t$  is the corrected thickness.

**Surface Composition Characterization.** X-ray photoelectron spectroscopy (XPS) data were collected by Axis Ultra (Kratos Analytical, Manchester, U.K.) under ultrahigh vacuum condition ( $<10^{-8}$  Torr), using a monochromatic  $\text{Al K}\alpha$  X-ray source (1486.6 eV), in the Surface Analysis Laboratory of CIME at EPFL. The source power was maintained at 150 W (10 mA, 15 kV). The emitted photoelectrons were sampled from a square area of  $750 \times 350 \mu\text{m}$ . Gold ( $\text{Au } 4f_{7/2}$ ) and copper ( $\text{Cu } 2p_{3/2}$ ) lines at 84.0 and 932.6 eV, respectively, were used for calibration, and the adventitious carbon 1s peak at 285 eV as an internal standard to compensate for any charging effects.

**Magnetic Measurements.** A SQUID magnetometer (MPMS XL-7, Quantum Design.) was used, and the studied mesoporous hematite films prepared at 700 and 800 °C were ground, forming powder samples that were wrapped into Teflon tape and put into the measuring chamber of the magnetometer. For both powdered samples, the hysteresis loops were measured in the applied fields ranging from  $-7 \text{ T}$  to  $+7 \text{ T}$  at temperatures of 5, 20, 50, 80, 150, 220, and 300 K. From the hysteresis loops, the temperature dependence of coercivity was evaluated as a tool for assessment and comparison of the size and substitution effects in studied systems. In addition, the zero-field-cooled (ZFC) and field-cooled (FC) magnetization curves were recorded on heating in the temperature range from 5 to 300 K and in an external magnetic field of 1000 Oe after cooling in a zero magnetic field and in a field of 1000 Oe, respectively.

**PXRD and Structure Refinement.** The powder X-ray data was acquired with a PANalytical X'Pert PRO in bragg-brentano geometry using  $\text{Cu K}\alpha$  radiation (1.540598 and 1.544423 Å, ratio 0.500), parallel polarization correction, and a graphite monochromator. The sintered  $\text{Fe}_2\text{O}_3$  was removed from the substrates using only mechanical force to preserve the structure of the material. This was performed by scraping the hematite layer with a razor blade taking care not to remove any of the substrate material. The removed hematite powder (ca. 5 mg) was then dispersed on a background-reducing and rotating single crystal silicon sample holder (slanting cut). Spectra were acquired from  $2\theta = 20 - 100^\circ$  at a step width

of  $0.017^\circ$ , 10 s per step. Only hematite peaks were observed in the spectra. Rietveld refinement was performed with JANA2006 with pseudo-Voigt peak fitting. The structure was refined with occupancy fixed at 1.0 and applying Berar's correction to obtain more realistic standard uncertainties. Bond distances were calculated with DIAMOND version 3.2c.

## Results and Discussion

Previous solution-based approaches to nanometer-sized  $\text{Fe}_2\text{O}_3$  have mainly used hydrolytic reactions in aqueous solvent systems to prepare colloidal solutions. One potential issue with the use of aqueous preparations of  $\text{Fe}_2\text{O}_3$  is the likelihood of passing through a hydroxyl-containing phase, like goethite ( $\alpha\text{-FeOOH}$ ). It has been demonstrated that the full removal of hydroxyls from hematite, upon conversion from goethite, requires temperatures over 800 °C.<sup>22</sup> For this reason, we sought a nonaqueous route to prepare hematite colloids. The dispersion of hematite nanoparticles (prepared by the gas-phase thermal decomposition of  $\text{Fe}(\text{CO})_5$ )<sup>23</sup> was achieved in a solution of 2-propanol with 1% (v/v) 2,4-pentanedione as a capping agent. Colloids remained nonturbid, indicating good particle dispersion, up to concentrations of ca. 100  $\text{mg mL}^{-1}$ . Combining this with the porogen hydroxypropyl cellulose (HPC) and the subsequent doctor blading onto conductive glass ( $\text{F}:\text{SnO}_2$  on quartz glass substrates) gave semitransparent films about 1  $\mu\text{m}$  thick before any thermal treatment. Films were then heated to 400 °C in air (10 h) to remove the organic phase, and a further sintering step in a tube furnace set to 700 or 800 °C (20 min) was performed. The mesoporous nature of the samples at different stages of the heat treatment can be seen clearly by the top-down scanning electron micrographs presented in Figure 1. Before annealing (Figure 1a), the original size of the  $\text{Fe}_2\text{O}_3$  nanoparticles can be observed (ca. 10 nm). After the removal of the organic porogen at 400 °C, the film (now ca. 500 nm thick by AFM) was found to be porous with necked particles in the 30 nm range (Figure 1b). This morphology is comparable to that observed with the

(22) Gualtieri, A. F.; Venturelli, P. *Am. Mineral.* **1999**, *84*, 895.

(23) Orthner, H. R.; Roth, P. *Mater. Chem. Phys.* **2002**, *78*, 453.



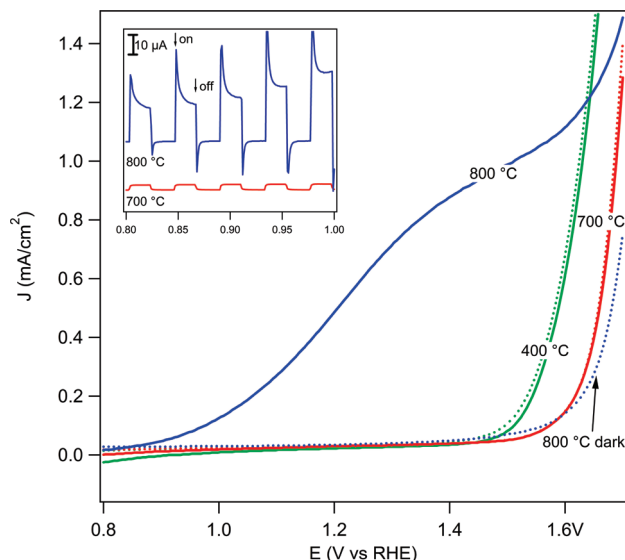


**Figure 2.** Electrochemical water oxidation current vs voltage curves of the photoanodes sintered at different temperatures in the dark (dotted curves) and under simulated solar light (solid curves, AM 1.5G 100 mW cm<sup>-2</sup>, spectrally corrected). The inset shows the photocurrent transient curves for the 700 and 800 °C sample created by chopping the light source during a current vs voltage sweep.

films prepared by an aqueous route.<sup>19</sup> The subsequent sintering at 700 or 800 °C provided films with morphology similar to the 400 °C case, but with larger feature size of the necked particles, ca. 60 and 75 nm (Figure 1c,d), respectively. The pore size correspondingly increased, and a slight decrease in the average film thickness to ca. 300 nm was observed by AFM (see Supporting Information).

The photoelectrochemical performance for these samples, with different sintering temperatures, is shown by sweeping current-potentiometry scans in 1 M NaOH electrolyte (pH 13.6) in the dark and with simulated solar illumination (AM 1.5G 100 mW cm<sup>-2</sup>) in Figure 2. The electrodes heated to 400 °C or even 700 °C showed no photocurrent, similar to the results obtained in previous work.<sup>19</sup> Moreover, based on the physical interpretation of photocurrent transients developed by Sanchez et al.,<sup>24</sup> the absence of transient photocurrent spikes near the expected photocurrent onset potential (Figure 2 inset) is consistent with transport processes that are limited by recombination in the bulk<sup>24</sup> or at grain boundaries as previously suggested.<sup>19</sup> However, upon the thermal treatment at 800 °C, a drastic change in performance occurs. The water oxidation photocurrent begins at about 900 mV versus RHE, rises to 0.56 mA cm<sup>-2</sup> at 1.23 V versus RHE ( $E_{\text{redox}}(\text{H}_2\text{O}/\text{O}_2)$ ) and passes 1.0 mA cm<sup>-2</sup> before the dark current onset (ca. 1.55 V vs RHE). In addition, the characteristic transient current spikes resulting from the accumulation of photogenerated holes at the SCLJ (due to the slow oxygen evolution reaction kinetics near the onset potential) are visible, suggesting that recombination in the bulk (or at grain boundaries) no longer limits charge carrier transport. This remarkable temperature dependence on the photoactivity was reproducible on many samples regardless of sintering atmosphere (air, oxygen, or argon) but provided that the heating time was under 30 min; for longer times at 800 °C the F:SnO<sub>2</sub> becomes insulating.<sup>25</sup> The thermal degradation of the F:SnO<sub>2</sub>

also accounts for the observed change in electrode dark current onset voltages: as the F:SnO<sub>2</sub> becomes more resistive, the dark current onset is pushed to more anodic voltages. In contrast, this shift of dark current onset was not observed for films prepared on quartz glass substrates with a sputtered Pt (200 nm) conducting layer, although the same temperature dependence of the photocurrent was observed. In addition, for samples prepared on Pt substrates, the photocurrent behavior after 1 h at 700 and 800 °C was identical to that of sintered samples for only 20 min (see Supporting Information). This indicates that the sintering temperature is a critical factor in the activity of hematite films prepared by this method. However, the relatively low photocurrent observed in the photoactive sample, as compared to the state-of-the-art hematite photoanodes,<sup>11</sup> is undoubtedly due to the large observed average feature size (75 nm) compared to the  $L_D$  of 2–4 nm. The film sintered at 400 °C exhibits a morphology that can potentially create significantly more photocurrent, but since the high sintering temperature that brings function to the 800 °C film also causes the sintering and growth of the hematite features to sizes far too large for high photocurrent production, the present method seems limited to the photocurrents observed. Therefore, there is a clear need to understand the origin of the established temperature effect to enable morphologies with smaller particle size to possess photoactivity.

Besides the particle size observed by SEM, an obvious difference between the electrodes could be seen optically by the color of the film. Films treated at 400 °C appeared more orange-red compared to the blood-red color of the films treated at 800 °C. The X-ray diffraction performed on the thin films as prepared showed only hematite and cassiterite (SnO<sub>2</sub>) phases present (see Supporting Information) and an expected decrease in the peak width of the hematite reflections as annealing temperature increased, due to the larger particle size. While quantum confinement effects have been observed in hematite with crystals having a smallest dimension of 5 nm,<sup>26</sup> its characterization as a charge-transfer insulator<sup>27</sup> suggests that quantum confinement effects should not be observed in the 30–75 nm particles which we observe here. Nevertheless, the absorption properties of hematite have reported to change as particle size<sup>28</sup> and shape<sup>29,30</sup> changes even up to 400 nm. Since the optical absorption properties and the electronic nature of the band gap in hematite is of great interest to understand its performance as a material for solar energy conversion, we investigated the optical properties with UV–vis spectroscopy. Figure 3a shows the absorption coefficient,  $\alpha$ , as a function of wavelength as calculated by the total (diffuse + direct) transmittance of the hematite films. In addition, typical electrodes sintered at the different temperatures but derived from the same doctor-bladed film are shown in the inset of Figure 3a. The absorption coefficient is characterized by a subband gap scattering tail of 600–750 nm which increases in intensity for the larger particle size. A sharp increase of the absorptivity

(24) Sanchez, C.; Sieber, K. D.; Somorjai, G. A. *J. Electroanal. Chem.* **1988**, 252, 269.

(25) Gordon, R. G. *MRS Bull.* **2000**, 25, 52.

(26) Vayssieres, L.; Sathe, C.; Butorin, S. M.; Shuh, D. K.; Nordgren, J.; Guo, J. H. *Adv. Mater.* **2005**, 17, 2320.

(27) Ma, Y.; Johnson, P. D.; Wassdahl, N.; Guo, J.; Skytt, P.; Nordgren, J.; Kevan, S. D.; Rubensson, J. E.; Böske, T.; Eberhardt, W. *Phys. Rev. B* **1993**, 48, 2109.

(28) Cornell, R. M.; Schwertmann, U. *The Iron Oxides: Structure, Properties, Reactions, Occurrences, And Uses*; 2nd ed.; Wiley-VCH: Weinheim, 2003.

(29) Fan, H. M.; You, G. J.; Li, Y.; Zheng, Z.; Tan, H. R.; Shen, Z. X.; Tang, S. H.; Feng, Y. P. *J. Phys. Chem. C* **2009**, 113, 9928.

(30) Wang, J.; White, W. B.; Adair, J. H. *J. Am. Ceram. Soc.* **2005**, 88, 3449.

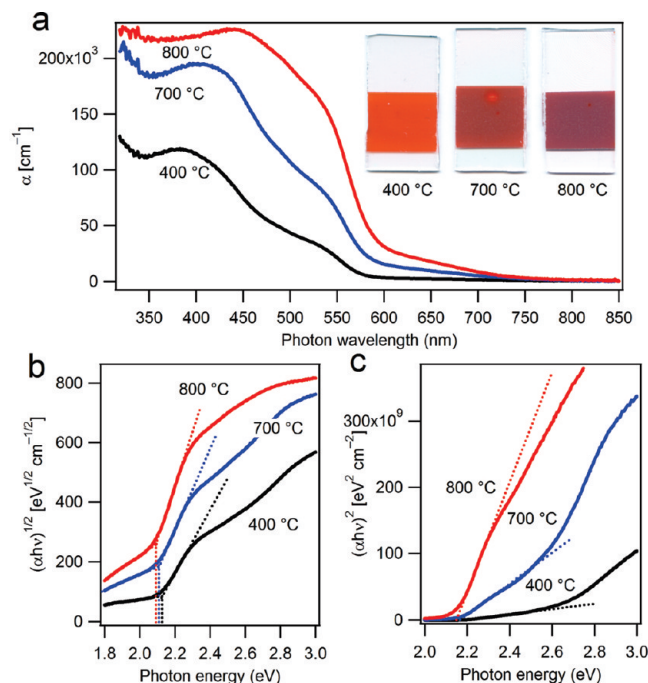


**Figure 3.** Optical properties of mesoporous hematite thin films. Panel a shows the absorption coefficient as a function of wavelength and the typical appearance of the electrodes (25 mm height, all derived from the same parent substrate). Tauc plots evaluating the optical band gap are shown for the indirect case in panel b and the direct case in panel c. A dotted line fitted to the linear portion of these plots shows the optical band gap approximation.

occurs at the band gap between 550 and 600 nm. Transitions in  $\alpha$  at 535 and 375 nm have been previously assigned to a ligand field ( ${}^6A_1 \rightarrow {}^4E$ ) and a ligand-to-metal charge transfer ( $6t_{1u} \rightarrow 2t_{2g}$ ) transitions, respectively.<sup>31</sup> Interestingly, the charge transfer transition at 375 nm in the sample heated to 400 °C is red-shifted in the samples heated to higher temperatures while the ligand field transition does not shift. In addition, the absorption coefficient increases with sintering temperature and, in the 800 °C sintered sample, exhibits a more full shape between these two transitions. Both the observations of charge transfer transition red shift and increase in  $\alpha$  have been previously observed in hematite with changing morphology (with constant preparation temperature), and could not be completely explained by the authors.<sup>29</sup> These changes cannot be attributed to size alone, as they are not typically observed in spherical nanoparticles with varied diameter.<sup>32</sup>

Further differences between the optical properties became evident by examining the band gap absorption onset. A Tauc analysis,<sup>33</sup> which assumes that the energy bands are parabolic with respect to the crystal momentum, most frequently indicates an indirect (phonon-assisted) band gap transition around 1.9–2.2 eV in hematite.<sup>6</sup> However, a few recent reports of a direct band gap have been attributed to quantum size-effects<sup>26,34</sup> or to an electrochemical deposition method.<sup>35,36</sup> The Tauc plots for an

indirect (i) and a direct (d) band gap are shown in Figure 3, panels b and c, respectively, and the band gap energies (determined by the intersection of the slopes on either side of the transition) are given in Table 1. A slight decrease in band gap was observed with increasing sintering temperature in both cases, and for the indirect case, the three electrodes exhibited similar-quality Tauc fits with band-gaps around 2.1 eV. In contrast, the direct transition is qualitatively better fit by the electrode sintered at 800 °C compared to the lower temperatures. This suggests a stronger direct transition and is consistent with reports of other hematite electrode sintered at high temperature,<sup>35,37</sup> and the strong increase observed in the ligand field transition at 535 nm. Interestingly, the slope of the transition increases with increasing temperature for both the indirect and the direct case. In the Tauc relation, the slope observed is proportional to the band tailing parameter,  $\beta$ , to the power 1/2 (i) or 2 (d).<sup>38</sup> Accordingly, the increase in slope is more dramatic in the direct band gap fit, and in both cases shows that  $\beta$  is increasing with sintering temperature. The band tailing parameter is related to the distribution of energy states near the valence and conduction bands and its increase is consistent with an increase in crystalline order and a larger particle size.<sup>39,40</sup> However, increasing the particle size and reducing the amorphous fraction alone cannot fully account for all of changes in the optical properties observed here. Nevertheless, these differences should have important implications on the performance of these photoanodes through the photogeneration of holes closer to the SCLJ. As such, further implications of the optical changes will be discussed later in context with the crystal structure results.

Another possible factor affecting the performance of hematite as a photoelectrode is an oxygen deficiency. Oxygen vacancies and the presence of hydroxyl groups play important roles in the electronic behavior of transition metal oxides, and are the most commonly present intrinsic defects found in hematite.<sup>41</sup> Samples of natural specular hematite even have been found to be degenerate semiconductors due to oxygen deficiencies.<sup>42</sup> It is unlikely in this case that a significant concentration of hydroxyl groups is present as our  $\text{Fe}_2\text{O}_3$  synthesis did not pass through a goethite ( $\alpha\text{-FeOOH}$ ) phase. Nevertheless, to examine the change in surface stoichiometry, X-ray photoelectron spectroscopy (XPS) was performed on the samples. The careful analysis of the Fe/O and the  $\text{Fe}^{2+/3+}$  ratios showed no statistically relevant evidence indicating that oxygen deficiency could be playing a role in the photoactivity of the electrode sintered at 800 °C. In fact, slightly more  $\text{O}^{2-}$  was found in the 800 °C case (the ratio Fe/O was found to be 0.802 and 0.748 based on atoms for the 400 and 800 °C samples, respectively). However, the XPS survey results gave an important clue as to the difference between electrodes. Figure 4 shows the results of the XPS survey. Surprisingly, peaks at binding energies of 27, 487, and 495 eV were found in the photoactive sample treated

(31) Marusak, L. A.; Messier, R.; White, W. B. *J. Phys. Chem. Solids* **1980**, *41*, 981.

(32) He, Y. P.; Miao, Y. M.; Li, C. R.; Wang, S. Q.; Cao, L.; Xie, S. S.; Yang, G. Z.; Zou, B. S.; Burda, C. *Phys. Rev. B* **2005**, *71*.

(33) Tauc, J.; Grigorov, R.; Vancu, A. *Phys. Status Solidi* **1966**, *15*, 627.

(34) Beermann, N.; Vayssieres, L.; Lindquist, S. E.; Hagfeldt, A. *J. Electrochem. Soc.* **2000**, *147*, 2456.

(35) Kleiman-Shwarsstein, A.; Hu, Y. S.; Forman, A. J.; Stucky, G. D.; McFarland, E. W. *J. Phys. Chem. C* **2008**, *112*, 15900.

(36) Schreiber, R.; Bello, K.; Vera, F.; Cury, P.; Munoz, E.; del Rio, R.; Meier, H. G.; Cordova, R.; Dalchle, E. A. *Electrochem. Solid-State Lett.* **2006**, *9*, C110.

(37) Hu, Y. S.; Kleiman-Shwarsstein, A.; Forman, A. J.; Hazen, D.; Park, J. N.; McFarland, E. W. *Chem. Mater.* **2008**, *20*, 3803.

(38) Sharma, P.; Vashistha, M.; Jain, I. P. *J. Optoelectron. Adv. Mater.* **2005**, *7*, 2647.

(39) Iribarren, A.; Castro-Rodriguez, R.; Sosa, V.; Pena, J. L. *Phys. Rev. B* **1998**, *58*, 1907.

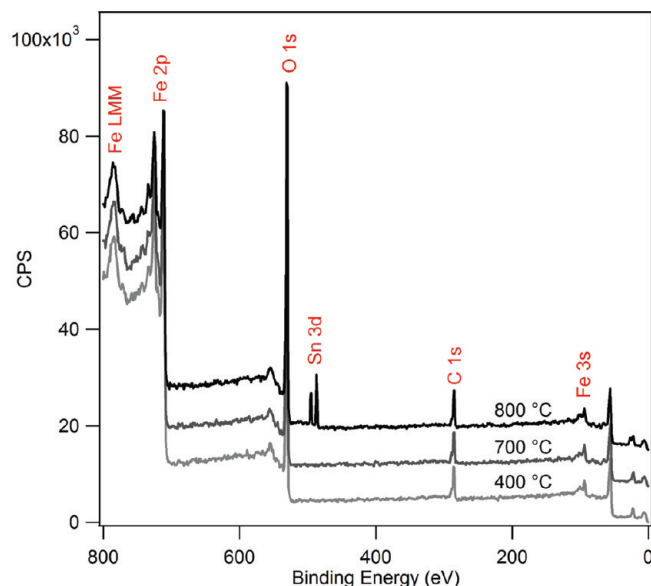
(40) Iribarren, A.; Castro-Rodriguez, R.; Sosa, V.; Pena, J. L. *Phys. Rev. B* **1999**, *60*, 4758.

(41) Gardner, R. F. G.; Tanner, D. W.; Sweett, F. J. *Phys. Chem. Solids* **1963**, *24*, 1183.

(42) Ahmed, S. M.; Leduc, J.; Haller, S. F. *J. Phys. Chem.* **1988**, *92*, 6655.

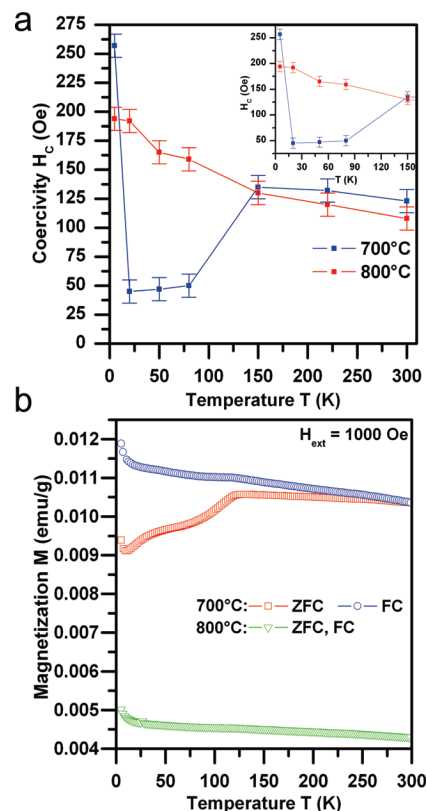
**Table 1.** Material Properties of Mesoporous Hematite Films<sup>a</sup>

sintering temperature	crystal size (nm)	optical band gap (eV)		lattice parameters (Å)		Fe–O bond distances (Å)		refinement reliability parameters		
		indirect	direct	a	c	short bond	long bond	$R_p$	$R_{wp}$	$R_{bragg}$
400 °C	27(2)	2.13	2.20	5.0349(4)	13.7511(13)	1.9491(69)	2.1068(32)	2.69%	3.71%	3.92%
700 °C	40(5)	2.11	2.17	5.0349(1)	13.7494(5)	1.9464(26)	2.1104(21)	2.42%	3.23%	3.06%
800 °C	44(4)	2.09	2.15	5.0350(2)	13.7484(5)	1.9453(29)	2.1120(42)	2.58%	3.45%	3.52%

<sup>a</sup> Standard uncertainties are given in parentheses.**Figure 4.** X-ray photoelectron spectroscopy survey data for the electrodes sintered at different temperatures. The plots are offset for clarity and the main peaks are identified.

at 800 °C but not the other samples. These peaks correspond to the 4d and 3d binding energies of Sn. This suggests that the Sn atoms could be diffusing from the substrate into the  $\text{Fe}_2\text{O}_3$  at the higher sintering temperature and acting as electron donating substitutional impurities ( $\text{Sn}^{4+}$ ). Indeed, while the deliberate introduction of impurities as dopants is not a requirement for photoactivity in  $\text{Fe}_2\text{O}_3$  (for samples prepared by spray pyrolysis or anodization of iron foils, for example),<sup>12,17,43,44</sup> n-type substitution has been determined to be very important for the photoactivity of hematite produced by various routes.<sup>45</sup> Atoms such as  $\text{Ti}^{4+}$ ,  $\text{Sn}^{4+}$ ,  $\text{Zr}^{4+}$ ,  $\text{Nb}^{5+}$ ,  $\text{Si}^{4+}$  and  $\text{Pt}^{4+}$  have been shown to have an effect on the photoactivity.<sup>10,37,46</sup> By doping at sufficient levels, high carrier conductivities can be attained. For example,  $\text{Zr}^{4+}$  was doped into single crystals to give donor densities on the order of  $10^{19} \text{ cm}^{-3}$ , conductivities around  $0.1 \Omega^{-1} \text{ cm}^{-1}$ , and increased electron mobility (perhaps due to an increase in dielectric constant) of  $0.1 \text{ cm}^2 \text{ V}^{-1} \text{ s}^{-1}$ .<sup>47</sup> Our XPS results gave 1.04 at % Sn based on metal in the photoactive sample, while none was detected in the sample sintered at 400 or 700 °C. In addition, for the samples prepared on Pt substrates, the Pt 4f peak was observed on the sample treated at 800 °C but not the others (0.65 at % Pt based on metal).

The XPS data give the plausible explanation that the elevated sintering temperature causes the migration of Sn from the

**Figure 5.** The magnetic properties of the hematite sintered at different temperatures. Panel a shows the temperature evolution of the coercivity and panel b shows the zero-field-cooled/field-cooled (ZFC/FC) curves for the nanostructured hematite films prepared at 700 and 800 °C.

substrate into the  $\text{Fe}_2\text{O}_3$  and results in an electronic modification of the mesoporous film. To strengthen this hypothesis and to collect further evidence of the differences in cation doping between the mesoporous hematite subjected to different sintering temperatures, we performed magnetic measurements of the films heated at 700 and 800 °C with a SQUID magnetometer. Figure 5a shows the temperature evolution of the coercivity,  $H_c$ , and Figure 5b shows the zero-field-cooled (FC) and zero-field-cooled (ZFC) magnetization curves recorded for both samples under an external magnetic field of 1000 Oe.

For the 800 °C sample, the coercivity monotonously decreases with the rise of the temperature following a general rule observed for nanosized systems. The mathematical extrapolation of the  $H_c$  versus  $T$  curve to higher temperatures (above 300 K) does not reach zero, clearly confirming no superparamagnetic behavior of the mesoporous film. This agrees well with the 30–50 nm size particles observed in the SEM as this range is above the critical diameter of ca. 10 nm required for observation of the superparamagnetic state at 300 K.<sup>48,49</sup> Taking into account

(43) Murthy, A. S. N.; Reddy, K. S. *Mater. Res. Bull.* **1984**, *19*, 241.(44) Mohapatra, S. K.; John, S. E.; Banerjee, S.; Misra, M. *Chem. Mater.* **2009**, *21*, 3048.(45) Kennedy, J. H.; Anderman, M.; Shinar, R. *J. Electrochem. Soc.* **1981**, *128*, 2371.(46) Goodenough, J. B. *Prog. Solid State Chem.* **1971**, *5*, 145.(47) Launay, J. C.; Horowitz, G. *J. Cryst. Growth* **1982**, *57*, 118.(48) De Grave, E.; Barrero, C. A.; Da Costa, G. M.; Vandenberghe, R. E.; Van San, E. *Clay Miner.* **2002**, *37*, 591.



the size of particles in the film, one would expect the appearance of the Morin transition temperature in the  $H_C$  versus  $T$  curve. An absence of this transition strongly implies a substitution effect in the structure of the hematite particles. The substitution of nonmagnetic cations in place of the high-spin  $\text{Fe}^{3+}$  ions can suppress the transition to the temperatures below even 5 K.<sup>48,49</sup> This is further confirmed by the ZFC and FC magnetization curves, which are identical, reversible, and exhibit no sign of the Morin transition temperature,  $T_M$  (indicating a substitution effect). Thus, hematite nanoparticles, featured in the 800 °C system, are probably all doped with  $\text{Sn}^{4+}$  ions which completely suppress  $T_M$  to below 5 K. From the quantitative viewpoint, it is known that the substitution of  $\text{Sn}^{4+}$  ions at concentrations of about 1 wt % results in the suppression of the Morin transition below 5 K.<sup>50</sup> This is consistent with the concentration found in the XPS study. In contrast, for the 700 °C sample, we observed a rather different behavior of the temperature dependence of  $H_C$  and the ZFC and FC magnetization curves. Just by comparing the values of the coercivity at 5 K for both studied samples, we can conclude that nanoparticles of the 700 °C sample are smaller than those of the 800 °C sample as the size of the particles is inversely correlated to their coercivity.<sup>51</sup> In addition, the measured temperature profile indicates a two-phase system as evidenced from the nonmonotonic character of the curve. This could be due to the presence of nonsubstituted hematite nanoparticles coexisting together with a fraction of hematite nanoparticles containing some degree of cation substitution. However, given that sintering for long times at 700 °C did not afford photoactivity to the hematite electrodes prepared on Pt substrates nor was any dopant found in the XPS survey of the electrode sintered at 700 °C, the amount of cation diffusion must be small at this sintering temperature. As the temperature of the magnetic measurement increases, the decline of coercivity is governed by a size effect originating from nonsubstituted nanoparticles. On further increase of the temperature, individual hematite nanoparticles with different degrees of substitution undergo the Morin transition at their respective characteristic temperatures. At 126 K, all nanoparticles have transitioned from antiferromagnetic to a weakly ferromagnetic state above the Morin transition temperature. The presence of the Morin transition at 126 K is also supported from the local maxima in both the ZFC and FC magnetization curves at ca. 120 K in the 700 °C sintered sample. Moreover, the ZFC/FC curves are highly irreversible implying a presence of small, undoped hematite nanoparticles, which exhibit a relaxation phenomenon. This is further indicated by the broad maximum at ca. 50 K in the ZFC curve which corresponds to the blocking temperature of single domain, undoped particles.<sup>52</sup>

The complete suppression of  $T_M$  in the electrode sintered at 800 °C and the observation of  $T_M$  at 126 K in the electrode sintered at 700 °C clearly demonstrate the significantly different degree of cation (Sn) substitution between these materials. This, along with the XPS data, confirms that the diffusion of dopant cations from the substrate at 800 °C is a major difference affecting the photoactivity of the anodes. In addition, the monotonic character of temperature dependence of coercivity

and ZFC/FC curves for the 800 °C sample implies a homogeneous distribution of tin cations in the entire mesoporous layer of the hematite film. On the other hand, the same magnetic analyses of the sample deposited at 700 °C indicate a two-phase system containing a combination of doped and undoped hematite particles, indicating that some diffusion of cations could be occurring at this temperature, but the incorporation of  $\text{Sn}^{4+}$  is not sufficient to be seen via XPS or afford photoactivity. Indeed, the sharp contrast between the dopant impurity concentration in the 700 and 800 °C electrodes is consistent with experimental results reporting the diffusion coefficient of cations in hematite.<sup>53</sup> Here, the diffusion coefficient was found to have an abrupt increase around 800–900 °C due to a transition in diffusion mechanism.

While the diffusion-doping of the  $\text{Fe}_2\text{O}_3$  at the higher sintering temperature provides a trivial explanation for the photoactivity of our hematite photoanodes, it does not explain the observed changes in the optical properties especially considering that other groups have reported the introduction of similar amounts of cations into the hematite lattice with no change in the optical properties.<sup>35,54</sup> In addition, recent work by Pailhé et al. showed that hematite exhibits changes in optical properties when heated to the equivalent temperatures.<sup>55</sup> Since the samples used in that work were bulk powders and not thin films on  $\text{SnO}_2$  substrates, it is unlikely that diffusion doping occurred. This implies that there is another fundamental underlying phenomenon influencing the optical properties of hematite. Since our application is to control the optical processes in hematite for the solar energy conversion, it is important to fully understand these phenomena. Indeed, the electrode sintered at 800 °C exhibited the smallest band gap, the highest absorption coefficient, and the most direct absorption onset. All of these attributes, in addition to photoactivity, would be beneficial to a hematite electrode with the ideal feature size of ca. 10 nm.

In the work of Pailhé et al. a change in hematite's reflectivity was correlated to structural transformations of the crystal lattice. Hematite crystallizes in the corundum structure (trigonal with space group  $R\bar{3}c$ ) with lattice parameters  $a = 5.0356 \text{ \AA}$ ,  $c = 13.7489 \text{ \AA}$ , and six formula units per unit cell.<sup>28</sup> It is easy to understand hematite's structure based on the packing of the anions,  $\text{O}^{2-}$ , which are arranged in a hexagonal closed-packed lattice along the [001] direction. The cations,  $\text{Fe}^{3+}$ , occupy the two-thirds of the octahedral interstices (regularly, with two filled followed by one vacant) in the (001) basal planes. The tetrahedral sites remain unoccupied. The arrangement of cations can also be thought of producing pairs of octahedra, linked by sharing a face parallel to the basal plane. In the [001] direction, these  $\text{Fe}_2\text{O}_9$  dimers form chains separated by an empty octahedral site. This pattern can be clearly seen in the hematite unit cell pictured in Figure 6. In addition, the face sharing of the octahedron dimers and the electrostatic repulsion of the  $\text{Fe}^{3+}$  cations are responsible for a trigonal distortion of the octahedron giving rise to  $C_{3v}$ -type symmetry. Consequently, there are two sets of Fe–O bond distances: the longer for bonds to the O atoms positioned on the shared face of the octahedra dimer. Figure 6 also shows the detail of a  $\text{Fe}_2\text{O}_9$  dimer and the different bonds. Upon sufficient thermal treatment of hematite, the crystallite size increases and the structure relaxes to maximize

(49) Vandenbergh, R. E.; Degraeve, E.; Landuydt, C.; Bowen, L. H. *Hyperfine Interact.* **1990**, 53, 175.

(50) Morrish, A. H. *Canted Antiferromagnetism: Hematite*; World Scientific: Singapore, 1994.

(51) Leslie-Pelecky, D. L.; Rieke, R. D. *Chem. Mater.* **1996**, 8, 1770.

(52) Dormann, J. L.; Fiorani, D.; Tronc, E. *Advances in Chemical Physics*; Prigogine, I., Rice, S. A., Eds.; John Wiley & Sons: New York, 1997; Vol. 98, p 283.

(53) Atkinson, A.; Taylor, R. I. *J. Phys. Chem. Solids* **1985**, 46, 469.

(54) Glasscock, J. A.; Barnes, P. R. F.; Plumb, I. C.; Savvides, N. J. *Phys. Chem. C* **2007**, 111, 16477.

(55) Pailhé, N.; Wattiaux, A.; Gaudon, M.; Demourgues, A. *J. Solid State Chem.* **2008**, 181, 2697.



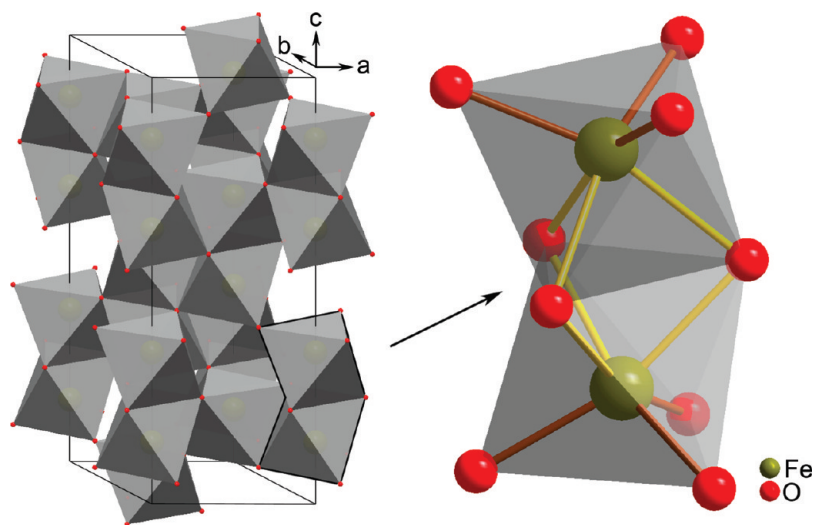


**Figure 6.** The unit cell (left) of hematite shows the octahedral face-sharing  $\text{Fe}_2\text{O}_9$  dimers forming chains in the  $c$  direction. A detailed view (right) of one  $\text{Fe}_2\text{O}_9$  dimer shows how the electrostatic repulsion of the  $\text{Fe}^{3+}$  cations produce long (yellow) and short (brown) Fe–O bonds.

the distance between the two iron cations in the  $\text{Fe}_2\text{O}_9$  dimers, optimizing the Madelung energy, and by consequence lengthening further the longer Fe–O bonds while contracting the shorter bonds. This structural distortion effect was further correlated by Pailhé et al. to the change in charge transfer optical transitions due to the increased  $t_{2g}$  orbital splitting induced by the  $C_{3v}$ -type distortion.

This provides a plausible explanation as to the origin of the drastic change in the optical properties of our mesoporous films, and in order to determine if a similar change in structure is also occurring with our material, a structural analysis was performed. To determine the structural properties of the different hematite samples, the hematite films were removed from the substrates and analyzed by XRD in powder form. The subsequent Rietveld refinement of the PXRD data with pseudo-Voigt peak fitting<sup>56</sup> gave the structural parameters and the refinement reliability factors<sup>57</sup> summarized in Table 1 along with the crystallite size as determined from the Scherrer equation. This latter data reveals the expected increase in crystallite size caused by the thermal treatment and clearly visible in the SEM images. However, despite the apparently significant increase in particle size between the samples heated at 700 and 800 °C in the SEM images, the PXRD data suggest that the crystallite size in these two samples is quite similar. This further suggests that grain boundaries between particles are not the determining factor for the performance of the hematite photoanodes in this case as a large increase in the crystallite size is expected if the grain boundaries are eliminated in the electrode heated to 800 °C.

The Rietveld refinement yielded a profile residual factor,  $R_p$ , of approximately 2.5% for each sample, suggesting very good quality refined models (data plots and fits are given in the Supporting Information). With respect to annealing temperature, the unit cell of hematite remained the same in the  $[100]$  and  $[010]$  directions (“ $a$ ” lattice parameter); however, a slight contraction of the unit cell was observed in the “ $c$ ” direction from 13.751 Å (400 °C) to 13.748 Å (800 °C). This is consistent with the relaxation of the structure previously observed,<sup>55</sup> and

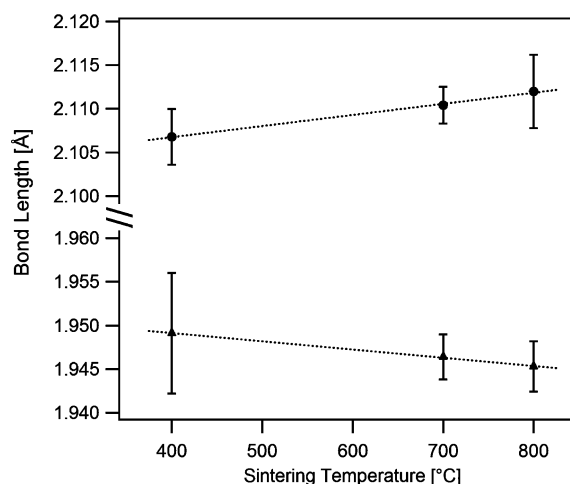


**Figure 7.** Evolution of the two different Fe–O bond lengths (circles for long bond and triangles for short) as a function of sintering temperature.

could not be a result of the incorporation of tin ions as the larger size of the  $\text{Sn}^{4+}$  cation (0.69 Å as compared to 0.65 Å for  $\text{Fe}^{3+}$ ) has been shown to increase the size of the unit cell in the  $c$  direction in hematite.<sup>58</sup> Moreover, this slight decrease in lattice constant is not expected to be a result of a decrease in lattice oxygen induced by the elevated sintering temperature as our previously discussed XPS results indicate a slightly higher oxygen content in the 800 °C sample. In addition, the refinement of the hematite structure<sup>59</sup> allowed the calculation of the Fe–O bond lengths. While the change of the bond lengths as a function of temperature is on the order of the error given by the structure refinement, the change is consistent with an increase in the trigonal distortion and structural relaxation previously observed.<sup>55</sup> Figure 7 graphically illustrates the evolution of the long and short Fe–O bond lengths as a function of sintering temperature. Here, we note that the linear shift of the bond lengths as a function of temperature suggests an even relaxation, which is not affected by incorporation of dopants. Overall, these

(56) Pailhé, N.; Majimel, J.; Pechev, S.; Gravereau, P.; Gaudon, M.; Demourgues, A. *J. Phys. Chem. C* **2008**, *112*, 19217.

(57) Young, R. A.; Prince, E.; Sparks, R. A. *J. Appl. Crystallogr.* **1982**, *15*, 357.

(58) Berry, F. J.; Greaves, C.; McManus, J. G.; Mortimer, M.; Oates, G. *J. Solid State Chem.* **1997**, *130*, 272.

(59) Blake, R. L.; Hessevic, R.; Zoltai, T.; Finger, L. W. *Am. Mineral.* **1966**, *51*, 123.

relatively small changes in structure have been shown to affect the optical properties of hematite and are remarkably the cause for a change in color of the material even well beyond the limit of quantum-confined domains.<sup>55</sup> Reasonably, they are also the cause for the increase of the absorptivity and band tailing parameter observed in our films as the amplification of the trigonal distortion directly influences the crystal field intensity and splitting and, consequently, the opto-electronic transitions exhibited by the material. Indeed, the observation of a shifting charge transfer transition at 375 nm here and not fully explained in work by Fan et al.<sup>29</sup> is consistent with an increase in the distortion, and further emphasizes the need for a detailed investigation of how the structural distortion affects the energy states and band structure as predicted by density functional theory. In addition, while Pailhé et al. suggested the particle size increase directly enabled the structural relaxation, it is not clear if the magnitude of the distortion can be controlled without increasing the particle size. This alone would be beneficial for the photoactivity of hematite as the increase in absorptivity would permit holes to be photogenerated closer to the SCLJ. Kinetically controlled heating methods like rapid thermal annealing may allow this.

Our observed correlation between the trigonal distortion and the optical properties provokes additional questions concerning the photoactivity of hematite in general. Most importantly, does the structural relaxation affect the photogenerated carrier lifetime, mobility, and reactivity toward water oxidation? While the current work correlates both the photoactivity and the change in the optical properties to the increase in the trigonal distortion in the structure, the onset of photoactivity can be attributed completely to the introduction of dopants through the diffusion from the substrate. However, in recent work on electrodeposited films of hematite, dopant atoms were directly incorporated into the film before annealing, but good photoactivity was not reported until heating at temperatures over 700 °C.<sup>35,37</sup> If we suppose that the incorporated dopant atoms are indeed acting as donors even when sintered at temperatures below 700 °C, this then suggests that the photoactivity of hematite does depend on the trigonal distortion. Then, if indeed this distortion is coupled to the particle size, it would help explain why many nanostructures of hematite consisting of feature sizes and morphologies that should produce high water-splitting photocurrents are generally poorly photoactive. The photoanodes prepared by APCVD or ultrasonic spray pyrolysis (USP) from our laboratory and others do, however, contain small feature sizes and exhibit high photoactivity. This would contradict the suggested link between the particle size, distortion, and photoactivity; however, both of these systems do also contain hematite which has a large crystalline domain. The individual platelets of the USP films are single crystal domains of ca. 500 nm in the [100] direction,<sup>12</sup> and the cauliflower structures created by the APCVD contain large domain particles sintered at the base and core of the structure.<sup>14</sup> These thick bases are topped by small particles which we have determined by high-resolution TEM to have the same crystalline orientation as the base probably due to an orientated attachment mechanism (unpublished result). In addition, Fan et al. observed optical changes similar to this work in anisotropic nanotubes with lengths varying up to 250 nm.<sup>29</sup> The evaluation of the trigonal distortion in hematite produced by these techniques would be interesting, but is complicated by the highly anisotropic form of the crystallites. On the other hand, it could be that the high temperatures reported in this and the other recent electrodeposition work is only necessary to fully incorporate the

donor dopant impurities onto cation sites in the lattice, and the temperature necessary coincidentally is the temperature which allows the structural relaxation. In contrast, the APCVD and USP methods perhaps effectively incorporate dopants during the synthesis of the hematite. Nevertheless, since the increase in the trigonal distortion does unambiguously correlate to a significant increase in absorption coefficient and improved band gap transition, important parameters for hematite photocatalysts, our future work will be directed toward decoupling the particle size, doping, and trigonal distortion in hematite to further understand its role in affecting the optoelectronic properties. In addition, since this work suggests a correlation between the structure and the optoelectronic properties we will seek to understand how the band structure and electronic transitions in hematite as calculated by density functional theory<sup>60</sup> are predicted to change with the structural relaxation. Combining these efforts will eventually realize hematite with the ideal morphology and high photoactivity.

## Conclusions

With this work, we have shown for the first time that relatively high water-splitting photocurrents can be obtained with mesoporous hematite photoanodes prepared by a solution-based colloidal method. Photoactivity was provided by annealing at 800 °C, which increased the particle size through sintering and drastically changed the optical properties of the film, increasing the absorption coefficient by up to a factor of 2. The cause of the surprising change in photoactivity and optical properties was further correlated to the incorporation of dopant ions as shown by XPS and magnetic investigation, and a structural distortion of the hematite lattice as shown by a refinement of XRD data. The latter effect suggests a new parameter which plays an important role in determining the optical properties, dopant incorporation, and photoactivity of hematite. Our work further indicates that the independent control over the crystal distortion, doping, and particle size will be necessary to achieve high efficiencies with hematite. Indeed, the complete understanding of how the structural properties of hematite influence its performance as a photoanode for water oxidation will ultimately allow for the efficient and sustainable storage of solar energy through water splitting.

**Acknowledgment.** We thank the Marie Curie Research Training Networks (Contract number MRTN-CT-2006-032474), the Swiss Federal Office of Energy (Project number 102326, PECHouse), the Ministry of Education of the Czech Republic (1M6198959201 and MSM6198959218) and the Academy of Sciences of the Czech Republic (KAN115600801) for financial support. We also acknowledge F. Bobard and M. Cantoni from the Centre Interdisciplinaire de Microscopie Electronique (CIME) at the EPFL for assistance in SEM imaging, N. Xanthopoulos from Centre Interdisciplinaire de Microscopie Electronique (CIME) at EPFL for surface XPS characterization, D. Logvinovich from the laboratory of crystallography (LCR) at EPFL for assistance with the XRD refinement, and S. C. Warren for helpful discussions.

**Supporting Information Available:** Data on samples prepared on Pt substrates, AFM images, and XRD profiles are presented. This material is available free of charge via the Internet at <http://pubs.acs.org>.

JA101564F

(60) Velez, J.; Bandyopadhyay, A.; Butler, W. H.; Sarker, S. *Phys. Rev. B* **2005**, *71*.